



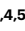






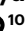




Weak self-induced cooling of tropical cyclones amid fast sea surface warming

Received: 24 January 2025

Accepted: 12 November 2025

Published online: 8 January 2026

 Check for updates

Shoude Guan ^{1,2,3,14}, Mengya Huang ^{1,14}, Wenju Cai ^{1,4,5,6} ,
Zhengguang Zhang ^{1,3}, I-I Lin ⁷ , Hyun-Sook Kim⁸, Lei Zhou ⁹,
Xiaopei Lin ^{1,3}, Zhao Xu^{1,3}, Fei-Fei Jin ¹⁰, Wei Mei¹¹, Qian Wang¹²,
Chun Zhou ^{1,2,3}, Ze Meng^{11,13}, Jiwei Tian ^{1,2,3} & Wei Zhao ^{1,2,3} 

Sea surface temperature directly beneath tropical cyclones is crucial for their intensification. In the long term, global warming heats the surface oceans, intensifying tropical cyclones, whereas concurrently with a cyclone, inner-core surface cooling is induced by the cyclone itself curtailing its intensification. However, the magnitude of cyclone-induced cooling, or the trend in storm-local sea surface temperature, remains uncertain. Here we provide a quantification using global surface drifter data from 1992 to 2021. We find that storm-local sea surface temperatures are rising at 0.29 ± 0.07 °C per decade—about twice the average rate in tropical cyclone-active regions despite enhanced cyclone-induced cooling; furthermore, the magnitude of cyclone-induced inner-core cooling is far smaller than previous estimates. The inner-core cooling measured by drifters is -0.68 ± 0.04 °C, substantially less than microwave satellite estimates (-1.05 ± 0.06 °C). State-of-the-art climate models tend to overestimate inner-core cooling while underestimating storm intensity. These findings offer observational benchmarks for models and suggest that current projections may underestimate the strength, frequency and impacts of major tropical cyclones.

Tropical cyclones (TCs) are among the most devastating natural disasters on Earth¹. Under greenhouse warming, TCs have been shifting towards higher intensities^{2–8}. The increasing TC intensity, combined with its poleward and coastal migration^{9–11}, poses rising risks to affected communities. Therefore, a better understanding of environmental factors controlling TC intensities and consequent improvements in forecasts and future projections to mitigate their impacts are of great importance to society¹². Among atmosphere–ocean factors, storm-local

sea surface temperature (SST) directly beneath TCs (defined as SST within 500 km around TC centre) is crucial as it determines TCs' enthalpy supply and thus is pivotal in controlling TC intensity^{13,14}. In recent decades, despite efforts to measure storm-local SST using fixed buoys, ship- or aircraft-based expendables^{15–23}, the collected observations have covered limited intense Category 1–5 TCs and mostly concentrated in the North Atlantic. Consequently, an understanding of storm-local SST on a global scale is not previously available.

¹State Key Laboratory of Physical Oceanography and Frontier Science Center for Deep Ocean Multispheres and Earth System (FDOMES)/Key Laboratory of Ocean Observation and Information of Hainan Province, Sanya Oceanographic Institution/Academy of Future Ocean, Ocean University of China, Qingdao, China. ²SANYA Oceanographic Laboratory, Sanya, China. ³Laboratory for Ocean Dynamics and Climate, Qingdao Marine Science and Technology Center, Qingdao, China. ⁴Laoshan Laboratory, Qingdao, China. ⁵State Key Laboratory of Loess and Quaternary Geology, Institute of Earth Environment, Chinese Academy of Sciences, Xi'an, China. ⁶State Key Laboratory of Marine Environmental Science and College of Ocean and Earth Sciences, Xiamen University, Xiamen, China. ⁷Department of Atmospheric Sciences, National Taiwan University, Taipei, Taiwan. ⁸Atlantic Oceanographic and Meteorological Laboratory, NOAA, Miami, FL, USA. ⁹State Key Laboratory of Submarine Geoscience and School of Oceanography, Shanghai Jiao Tong University, Shanghai, China. ¹⁰Department of Atmospheric Sciences, SOEST, University of Hawaii at Manoa, Honolulu, HI, USA. ¹¹Department of Atmospheric and Oceanic Sciences & Institute of Atmospheric Sciences, Fudan University, Shanghai, China. ¹²National Meteorological Centre, China Meteorological Administration, Beijing, China. ¹³Shanghai Typhoon Institute, China Meteorological Administration, Shanghai, China. ¹⁴These authors contributed equally: Shoude Guan, Mengya Huang. ✉e-mail: cwjresearch@gmail.com; iilin@ntu.edu.tw; weizhao@ouc.edu.cn

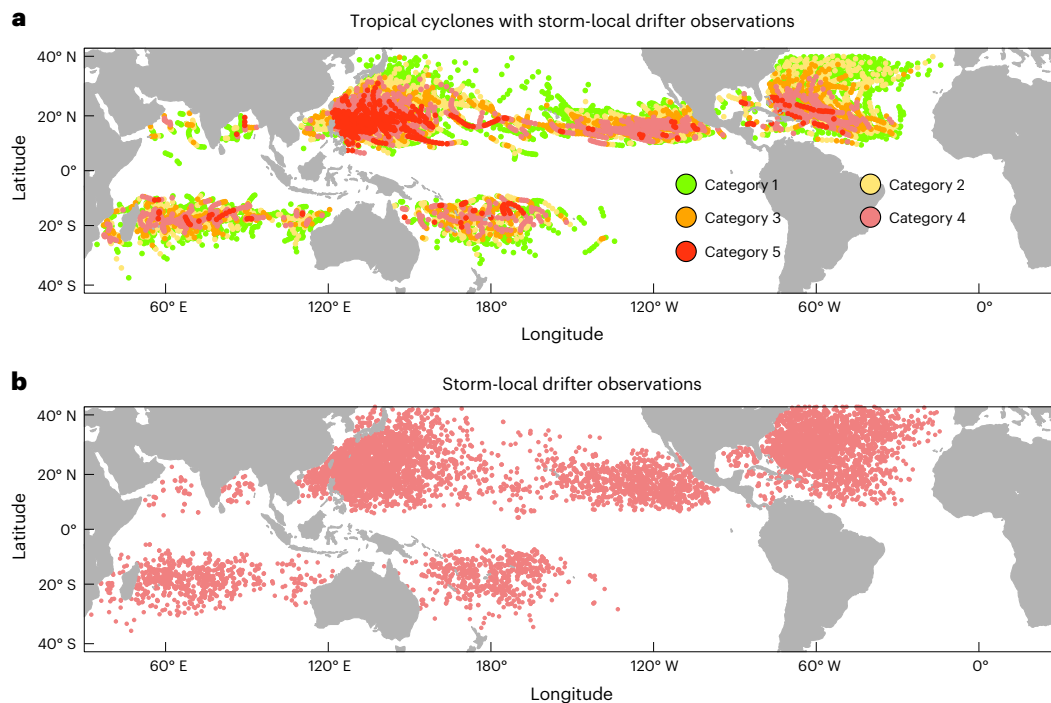


Fig. 1 | Identified drifter observations and corresponding tropical cyclones. Storm-local sea surface temperature and cooling observations are identified by pairing drifters with tropical cyclones. **a**, Global distribution of Category 1–5 tropical cyclones paired with drifters. **b**, Identified storm-local sea surface temperature and cooling observations within a 500-km radius from storm

centres. In total, 32,801 storm-local drifter samples are identified, which capture 77% of Category 1–5 tropical cyclones. The distribution of storm-local samples overlaps reasonably well with the distribution of global tropical cyclones with a strong correlation reaching 0.82 ($P = 8.35 \times 10^{-89}$ based on a two-sided Student's *t*-test). Basemaps generated using M_Map v1.4 (www.eoas.ubc.ca/~rich/map.html).

The warm tropical ocean serves as an energy source for TCs. Under greenhouse warming, the SST warming trend averaged over TC-active tropics during TC seasons has been estimated and used as an indicator to explore the TC intensity increase^{1,2,14}. However, the mean SST does not account for variabilities of TC tracks^{9–11} and self-induced SST cooling²⁴, making it different from storm-local SST that TCs directly experience. The storm-local SST is reduced by TC-enhanced turbulent vertical mixing, primarily through entraining subsurface cold water into surface layers^{24–27}. Due to a strengthening of upper ocean thermal stratification, the cooling effect is projected to be enhanced²⁸, potentially offsetting the conductive effect of greenhouse warming on the storm-local SST trend.

Moreover, the TC-induced storm-local SST cooling reduces the ocean's enthalpy supply and suppresses TC intensification on synoptic timescales, a phenomenon known as negative feedback²⁴. Although the concept was proposed nearly half a century ago²⁹, the magnitude and spatial pattern of storm-local SST cooling remain largely unknown. The lack of this knowledge is because most previous studies focused on individual TCs by in situ observations^{15–23}, which are difficult to obtain, or composite cooling by microwave satellite observations^{27,30}. Whereas microwave radiometers offer accurate SST observations under cloud coverage, their accuracy is compromised by attenuation and scattering of microwave signals by heavy raindrops³¹. Thus, microwave satellites can provide SST cooling several days after TCs (that is, cold wake), but they cannot provide accurate storm-local SST cooling. Lack of understanding of storm-local SST cooling hinders improvement of TC intensity forecasts and projections²¹.

Quantifying the storm-local SST trend and the synoptic storm-local SST cooling has been a long-standing challenge due to a scarcity of reliable observations in harsh TC conditions. Here we overcome the issue by identifying over 32,000 storm-local SST and cooling observations for Category 1–5 TCs from global drifters during 1992–2021. Using these data, we find that the storm-local SST is warming faster than the mean

warming rate in TC-active regions and that the TC-induced storm-local cooling is far smaller than commonly suggested based on microwave satellite observations and in High Resolution Model Intercomparison Project (HighResMIP) experiments of Coupled Model Intercomparison Project Phase 6 (CMIP6).

Storm-local SST from pairing drifters with TCs

Drifters started to be deployed over global oceans by the Global Drifter Program in 1979. To date, more than 25,000 drifters have been deployed, providing over 40 million SST records. During their Lagrangian drift following surface currents, drifters intersect with TCs and record SSTs beneath TCs reliably. Importantly, these drifters provide SST records at 6-hourly intervals at 00, 06, 12 and 18 Coordinated Universal Time (UTC)³², coinciding with the timing of global TC tracks from the International Best Track Archive for Climate Stewardship (IBTrACS) database ('TC datasets' in Methods).

The data allow an exact temporal match between drifter-observed SSTs and TCs to identify storm-local SSTs. By subtracting pre-TC SST from the storm-local SST, we calculate TC-induced storm-local SST cooling (Extended Data Fig. 1). Similarly, we calculate cold wakes left by TCs. When pairing the storm-local or post-TC SST with pre-TC SST, a criterion of drifting distance less than 100 km is set. Changing the criterion to 50 km or 150 km has little difference to the cooling estimates (Extended Data Fig. 2a). Moreover, a composite analysis finds that impacts of mesoscale processes on the cooling estimate are negligible, supported by sensitivity tests using a Lagrangian approach and a current velocity criterion (Extended Data Figs. 2b,c) ('Storm-local SST and cooling' in Methods).

Given that the vast majority of damage and mortalities are associated with intense TCs, we focus on Category 1–5 TCs. We identify 32,801 storm-local SST and cooling observations over the past three decades, associated with 1,024 global Category 1–5 TCs (Fig. 1a,b). During this period, 1,324 Category 1–5 TCs developed in global oceans, meaning

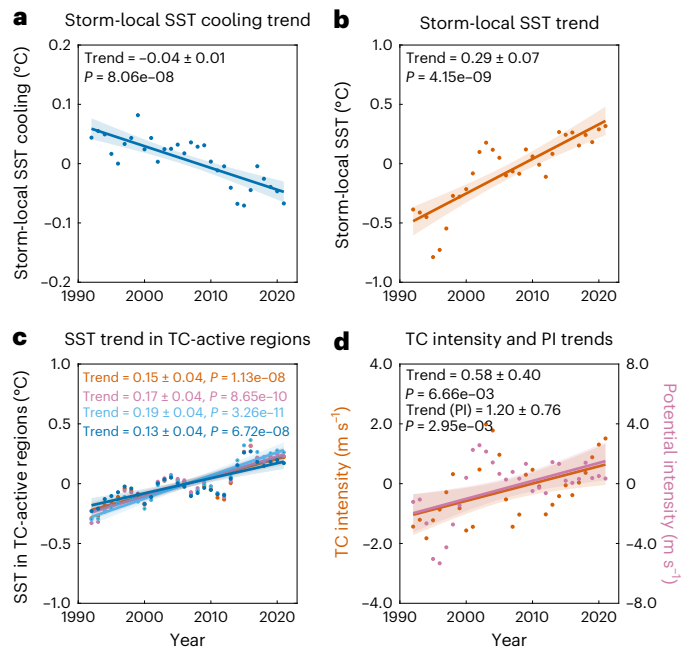


Fig. 2 | Warming trend of storm-local SST and intensifying tropical cyclones. **a, b**, Storm-local SST cooling (blue) and SST (red) trends from drifter observations. **c**, Mean SST trend in tropical cyclone (TC)-active regions from monthly ORASS (red), ERA5 (purple), ERSST (light blue) and HadISST (dark blue) datasets. **d**, Trend in drifter-captured TC intensity from the IBTrACS (red) and trend in potential intensity (PI) (purple) calculated based on storm-local drifter SSTs. A similar TC intensity trend is obtained using a homogenized Advanced Dvorak Technique Hurricane Satellite dataset³. In all panels, values are normalized, and then a 3-year running average is applied. Lines show linear regressions, with shadings denoting the 95% confidence intervals and labels denoting trends \pm the 95% confidence intervals ($^{\circ}\text{C}$ per decade for **a–c** and m s^{-1} per decade for **d**) and P values based on a two-sided Student's t -test. Storm-local SST is warming faster than the mean warming rate in TC-active regions, indicating that intense TCs are more likely to travel over regions experiencing faster warming than the broad tropics.

that drifter observations overlap with approximately 77% of the TCs or 64% of 6-hourly TC trackpoints. Global distributions of the identified storm-local observations overlap reasonably well with distributions of global TCs with a strong correlation reaching 0.82 ($P < 0.01$). We use such a quantity of in situ observations to determine the storm-local SST trend in the past three decades and to characterize the TC-induced storm-local SST cooling.

Fast-warming trend of storm-local SST

On a global average, TC-induced storm-local SST cooling is enhancing at -0.04 ± 0.01 $^{\circ}\text{C}$ per decade during 1992–2021 (Fig. 2a), which is probably linked to the increasing TC intensity³ and strengthening ocean thermal stratification²⁸. This trend is close to an increasing trend of cold wake reported by ref. 33. Despite the enhanced cooling, TCs have been experiencing a fast warming in storm-local SST at 0.29 ± 0.07 $^{\circ}\text{C}$ per decade ($P < 0.01$) (Fig. 2b). This means that the minimal enhancement in the TC-induced cooling effect cannot offset the conductive warming effect of ongoing global warming, leading to an increasing trend of storm-local SST.

Furthermore, we find that the storm-local SST warming is approximately twice as fast as that of the previously perceived mean SST warming in TC-active regions (Extended Data Fig. 3 and ‘SST in TC-active regions’ in Methods). The mean warming rate in TC-active regions, conventionally used as an indicator for exploring TC intensity change under greenhouse warming², is $0.13\text{--}0.19 \pm 0.04$ $^{\circ}\text{C}$ per decade (Fig. 2c). We obtain consistent storm-local SST and TC-active region SST

trends by reducing drifter observations and projecting tropical SST to drifter observations (‘Linear trend detection’ in Methods). Thus, TCs are more likely to travel in faster-warming regions in recent decades. Dynamically, considering that tropical SST exhibits large gradients but convection homogenizes high-tropospheric temperatures, regions warming faster than the broad tropics are more likely to sustain deep convection for intense TCs^{34–36}.

In theory, higher SST should fuel more intense TCs (ref. 1). Historical records reveal that corresponding TC intensity is increasing at 0.58 ± 0.40 m s^{-1} per decade ($P < 0.01$) (Fig. 2d). To examine the effect of the storm-local SST warming trend on the TC intensity increase, we calculate a trend of potential intensity (PI) (‘Potential intensity’ in Methods). The parameter PI refers to the maximum intensity that a TC can achieve and is widely used to project TC activities under greenhouse warming^{37–39}. The PI trend (Fig. 2d), calculated based on storm-local SST, shows an increasing trend of 1.20 ± 0.76 m s^{-1} per decade ($P < 0.01$). On the basis of the PI trend, we estimate a theoretical expectation of the TC intensity trend of 0.60 m s^{-1} per decade using a method proposed by ref. 6 (‘PI-derived intensity trend’ in Methods). The result aligns closely with the observed trend, suggesting that the fast-warming trend of storm-local SST plays an important role in fuelling intense TCs.

Far weaker storm-local cooling than suggested by satellites

By modulating enthalpy flux from oceans to TCs, TC-induced storm-local SST cooling is a key determinant of TC intensification on the synoptic timescale^{15,23}. In this section, we characterize the magnitude and spatial pattern of TC-induced storm-local cooling by compositing global drifter observations. Despite microwave satellite SSTs being widely used as substitutes when in situ data are unavailable^{27,30}, they suffer attenuation under heavy rainfall in storm-local conditions³¹. As such, we quantify their uncertainties in observing storm-local SST cooling through a comparison with drifter observations. To explore the temporal evolution of TC-induced SST cooling, we identify over 1,500,000 drifter observations from 5 days before to 5 days after TC passage, yielding approximately 30,000 observations per synoptic hour (00, 06, 12 and 18 UTC).

Drifter observations capture a typical rightward (leftward) shift of the maximum SST cooling in the northern (southern) hemisphere, attributed to wind-current resonance to the right (left) of TC tracks²⁴ (Fig. 3a,b). The spatial pattern of SST cooling in the northern hemisphere resembles that in ref. 23 based on fixed buoy observations. The maximum cooling shift to the right or left is approximately 75 km. In the along-track direction, storm-local SST cooling peaks about 200 km behind TCs. Compared to the maximum cooling far from TCs, cooling located within high wind inner-core areas (typically within 100 km of TC centres, referred to as inner-core SST cooling hereafter), where most enthalpy flux occurs, is a critical control on TC intensity^{15,15,23,38}. An inner-core SST cooling of -0.5 $^{\circ}\text{C}$ is sufficient to suppress TC intensification⁴⁰.

On the basis of drifter observations, we find that the spatial extent of -0.5 $^{\circ}\text{C}$ cooling covers almost the entire inner-core region, with an average inner-core SST cooling of -0.68 ± 0.04 $^{\circ}\text{C}$, which can exert a noticeable negative effect on TC intensity. We calculate an average cooling by weighting drifter-observed cooling in each $5^{\circ} \times 5^{\circ}$ grid, according to actual number of TCs. The weighted average of inner-core SST cooling is of comparable magnitude to that obtained by directly averaging all storm-local drifter observations, of -0.65 $^{\circ}\text{C}$ vs -0.68 $^{\circ}\text{C}$.

To compare storm-local SST cooling observed by microwave satellites with that observed by drifters, we interpolate gridded microwave satellite SST onto the location of drifter observations (‘Comparing microwave satellite data with drifters’ in Methods). Under TC high winds, the upper ocean from surface to O (100 m) depth is well mixed, and diurnal warming disappears⁴¹. Consequently, both

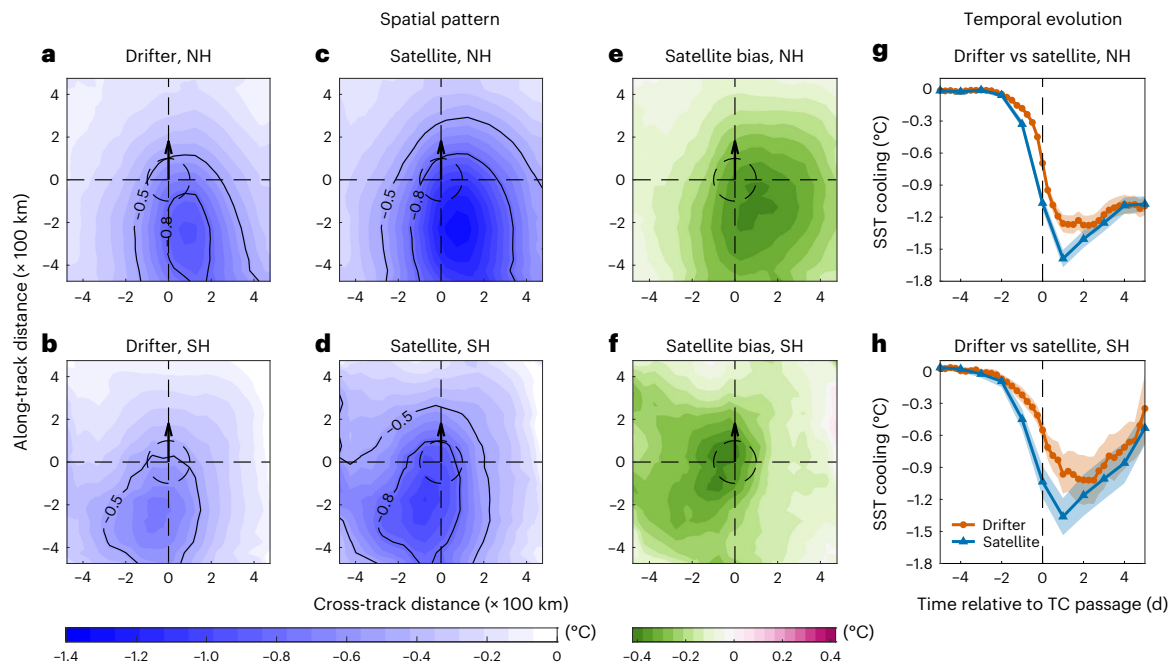


Fig. 3 | Tropical cyclone-induced sea surface cooling and overcooling in microwave satellite observations. **a, b**, Spatial pattern of storm-local SST cooling based on drifter observations in the northern and southern hemisphere (NH and SH). Contours of $-0.5\text{ }^{\circ}\text{C}$ and $-0.8\text{ }^{\circ}\text{C}$ are shown, with arrows denoting cyclones' moving direction and dashed circles denoting the inner-core area. **c, d**, Same as **a, b**, but based on microwave satellite observations. **e, f**, Same as **a, b**,

but for cooling bias of microwave satellite observations. **g, h**, Temporal evolutions of average cooling within 100 km of storm centres from drifter (red) and microwave satellite observations (blue) in the NH and SH. Shadings represent the 95% confidence intervals. Vertical dashed lines indicate the time of TC passage. On average, inner-core cooling is $-0.68 \pm 0.04\text{ }^{\circ}\text{C}$. Whereas microwave satellite data accurately capture cold wakes, they overestimate the inner-core cooling by 55%.

microwave satellites and drifters measure foundation SST, enabling a valid comparison.

We find that the projected microwave satellite data substantially overestimate the storm-local SST cooling (Fig. 3c–f). For example, $-0.5\text{ }^{\circ}\text{C}$ contours derived from microwave satellite observations are about 250 km ahead of those from drifter observations in the along-track direction, with $-0.8\text{ }^{\circ}\text{C}$ contours spreading across the inner-core region. Quantitatively, average inner-core SST cooling by microwave satellites is $-1.05 \pm 0.06\text{ }^{\circ}\text{C}$, showing an overestimation of $-0.37 \pm 0.04\text{ }^{\circ}\text{C}$ (55%) ($P < 0.01$) (Fig. 3g, h).

Gridded microwave satellite data reveal a consistent cold bias of inner-core SST cooling with the projected microwave satellite data (Extended Data Fig. 4). Such a large cold bias can result in a 22% underestimation of enthalpy flux ('Enthalpy flux' in Methods). The overestimation of inner-core SST cooling by microwave satellite data is also supported by independent moored buoys in global TC-active basins (Extended Data Fig. 5). In individual TC-active basins, including the North Atlantic (NA), Eastern North Pacific (ENP), Western North Pacific (WNP), South Indian (SI) and South Pacific (SP), the cold bias consistently emerges (Extended Data Fig. 6). Moreover, for weak TCs such as tropical depressions and tropical storms, microwave satellite observations still overestimate the inner-core SST cooling by about 30% and 50%, respectively (Extended Data Table 1).

We compare temporal evolution between drifter- and satellite-observed SST cooling (Fig. 3g, h and Extended Data Fig. 4). TC-induced SST cooling emerges 2 days before TC passage (Day₋₂), peaks on the day right after TC passage (Day₊₁) and gradually recovers afterward. Microwave satellite observations show overestimations in SST cooling from Day₋₁ to Day₊₁. However, the cold wake afterwards is accurate. The results indicate that while microwave satellite data exhibit a systematic cold bias directly beneath TCs, they can reliably capture the cold wake after TCs. Additionally, the systematic cold bias does not substantially impact trends.

Corresponding to surface cooling, TC-enhanced mixing also results in subsurface warming (that is, ocean heat pumping by TCs), potentially influencing global climate⁴². The overestimations of SST cooling revealed here, however, suggest that the heat pumping estimated from microwave satellites would be overestimated. This estimation does not account for the vast vertical mixing driven by deep penetration of near-inertial waves, which warms the permanent thermocline without cooling the surface⁴³. Thus, we recommend using microwave satellite SSTs for trend and cold wake studies, but caution is advised when examining inner-core SST cooling or assimilating such data into TC models.

Overcooling contributes to weak TCs in CMIP6 models

To date, climate models tend to produce an underestimated TC intensity, especially for major (Category 3–5) TCs (refs. 12, 44, 45). The underestimation is previously attributed to multiple factors, including model physics and parameterization, low model resolution and uncertainties in TCs' interaction with environments^{46–48}. Given the critical role that inner-core SST cooling plays in controlling TC intensification^{13, 15, 23}, we evaluate performances of coupled TC models in simulating the inner-core SST cooling and TC intensity, using outputs from five high-resolution models of the HighResMIP experiments of CMIP6 (ref. 49) ('Model simulations' in Methods).

Despite the cooling pattern being generally simulated, there is an overestimation of the modelled inner-core SST cooling and an underestimation of the modelled TC intensity ($P < 0.01$) (Fig. 4a, b and Extended Data Fig. 7). The overcooling consistently exists in individual TC-active basins, including the NA, ENP, WNP, SI and SP, with a global average cooling of $-1.38 \pm 0.02\text{ }^{\circ}\text{C}$ and a cold bias of $-0.70 \pm 0.10\text{ }^{\circ}\text{C}$ (103%, $P < 0.01$). In association, TC intensity is underestimated by $10.53 \pm 0.26\text{ m s}^{-1}$ ($P < 0.01$). When comparing cooling with the same TC attributes in the WNP TC main development region,

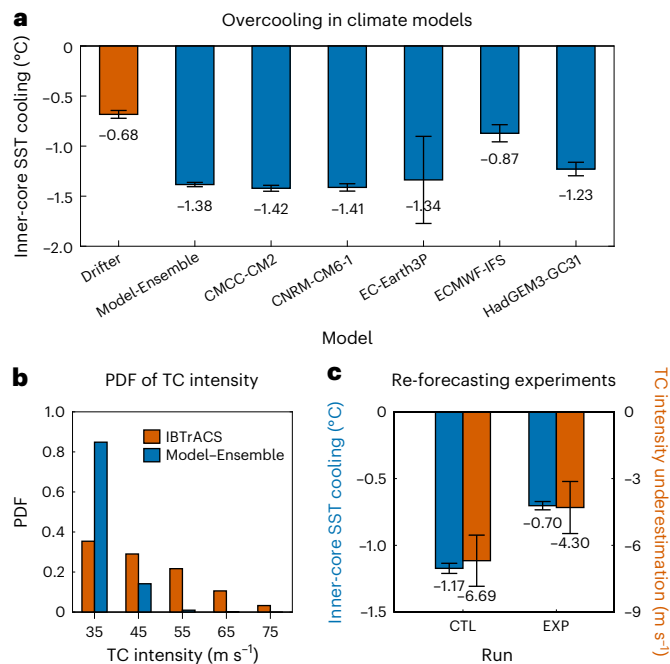


Fig. 4 | Overcooling and accompanying tropical cyclone intensity underestimation in models. **a**, Average inner-core SST cooling as observed (red, $n = 1,328$), simulated by Model-Ensemble and individual HighResMIP models of CMIP6 (blue, $n = 7,599; 4,190; 2,524; 41; 264$ and 580). **b**, Probability density function (PDF) of TC intensity from the IBTrACS records (red) and the HighResMIP Model-Ensemble (blue). **c**, Comparison of average inner-core SST cooling (blue) and TC intensity underestimation (red) between control (CTL, $n = 1,783$) and experimental (EXP, $n = 1,990$) runs without and with a reduced inner-core cooling, respectively, based on the COAWST model. In all panels, bars and error bars indicate mean and the corresponding 95% confidence interval values. All model outputs within CMIP6 are from high-resolution experiments. Climate models overestimate inner-core cooling and underestimate tropical cyclone intensity. Reducing this cold bias increases average cyclone intensity.

the overcooling is also produced (Extended Data Figs. 8a–g) ('Overcooling in CMIP6 high-resolution models' in Methods). Moreover, the overcooling consistently occurs for TCs from tropical depression to Category 4—the maximum intensity that the models can simulate (Extended Data Fig. 8h).

Theoretically, the overcooling reduces the enthalpy supply from oceans to TCs, thereby impeding TC intensification⁴⁷. Hence, in addition to the known factors^{46–48}, the overestimated inner-core SST cooling is a potential contributor to the modelled TC intensity underestimation. To illustrate the effect of overcooling, we compare average TC intensity in runs with (referred to as experimental runs) and without (referred to as control runs) a reduced inner-core SST cooling, using the Coupled-Ocean-Atmosphere-Wave-Sediment Transport (COAWST) modelling system⁵⁰ ('Model simulations' in Methods). The reduced cooling is achieved by reducing vertical mixing (with other conditions unchanged) because it dominantly controls the inner-core SST cooling²⁴. In this process, 22 TCs are re-forecasted and up to 2,000 hourly TC track points are generated, of which simulated tracks are consistent (Extended Data Fig. 9). On average, the model achieves a reduction in the inner-core SST cooling from -1.17 ± 0.04 °C to -0.70 ± 0.03 °C (Fig. 4c), comparable to the drifter-observed value. Correspondingly, the average TC intensity underestimation is reduced by 36% from -6.69 ± 1.15 m s⁻¹ to -4.30 ± 1.17 m s⁻¹.

Thus, we identify a substantial overestimation of inner-core SST cooling that probably contributes considerably to the underestimation of modelled and predicted TC intensity. Addressing the overcooling

and other known factors, such as model physics and parameterizations, low model resolution, uncertainties in TCs' interaction with dry air, environmental wind shear, trough/ridges and land, is important for improving TC intensity forecasts and projection^{46–48}.

In summary, we find that TCs are experiencing a fast-warming trend of storm-local SST at a rate of 0.29 ± 0.07 °C per decade during 1992–2021. The warming rate is much faster than the mean warming rate in TC-active regions. The faster storm-local warming provides observational evidence that TCs since the 1990s could have already been partially fuelled by greenhouse warming and suggests that intense TCs are more likely to occur in regions experiencing faster warming than the mean warming over TC-active regions. Importantly, despite an anticipated enhancement in the TC-induced cooling effect on the synoptic timescale, the TC-induced inner-core SST cooling averaged over the period is -0.68 ± 0.04 °C, far smaller than the commonly suggested but overestimated value of -1.05 ± 0.06 °C from microwave satellite observations. CMIP6 high-resolution models also overestimate the inner-core SST cooling. By reducing the inner-core SST cooling in the ocean component of a modelling system, we find an increase in average TC intensity. Thus, our finding provides a fundamental observational benchmark for models and prediction systems. Further, our result suggests that the cold bias in coupled climate models probably contributes to an underestimate in projections of major TC frequency, with a commensurate underestimation in the associated risks of extreme rainfall, high sea levels and socio-economic impacts under greenhouse warming.

Online content

Any methods, additional references, Nature Portfolio reporting summaries, source data, extended data, supplementary information, acknowledgements, peer review information; details of author contributions and competing interests; and statements of data and code availability are available at <https://doi.org/10.1038/s41561-025-01879-x>.

References

- Emanuel, K. Increasing destructiveness of tropical cyclones over the past 30 years. *Nature* **436**, 686–688 (2005).
- Webster, P. J., Holland, G. J., Curry, J. A. & Chang, H. R. Changes in tropical cyclone number, duration, and intensity in a warming environment. *Science* **309**, 1844–1846 (2005).
- Kossin, J. P., Knapp, K. R., Olander, T. L. & Velden, C. S. Global increase in major tropical cyclone exceedance probability over the past four decades. *Proc. Natl Acad. Sci. USA* **117**, 11975–11980 (2020).
- Wang, G., Wu, L., Mei, W. & Xie, S. P. Ocean currents show global intensification of weak tropical cyclones. *Nature* **611**, 496–500 (2022).
- Knutson, T. R. et al. Tropical cyclones and climate change. *Nat. Geosci.* **3**, 157–163 (2010).
- Kossin, J. P., Olander, T. L. & Knapp, K. R. Trend analysis with a new global record of tropical cyclone intensity. *J. Clim.* **26**, 9960–9976 (2013).
- Mei, W. & Xie, S. P. Intensification of landfalling typhoons over the northwest Pacific since the late 1970s. *Nat. Geosci.* **9**, 753–757 (2016).
- Klotzbach, P. J. et al. Trends in global tropical cyclone activity: 1990–2021. *Geophys. Res. Lett.* **49**, e2021GL095774 (2022).
- Kossin, J. P., Emanuel, K. A. & Vecchi, G. A. The poleward migration of the location of tropical cyclone maximum intensity. *Nature* **509**, 349–352 (2014).
- Wang, S. & Toumi, R. Recent migration of tropical cyclones toward coasts. *Science* **371**, 514–517 (2021).
- Murakami, H. et al. Detected climatic change in global distribution of tropical cyclones. *Proc. Natl Acad. Sci. USA* **117**, 10706–10714 (2020).

12. Balaguru, K. et al. Ocean barrier layers' effect on tropical cyclone intensification. *Proc. Natl Acad. Sci. USA* **109**, 14343–14347 (2012).
13. Schade, L. R. Tropical cyclone intensity and sea surface temperature. *J. Atmos. Sci.* **57**, 3122–3130 (2000).
14. Bhatia, K. et al. A potential explanation for the global increase in tropical cyclone rapid intensification. *Nat. Commun.* **13**, 6626 (2022).
15. Cione, J. J. & Uhlhorn, E. W. Sea surface temperature variability in hurricanes: implications with respect to intensity change. *Mon. Weather Rev.* **131**, 1783–1796 (2003).
16. Black, P. G. et al. Air–sea exchange in hurricanes: synthesis of observations from the coupled boundary layer air–sea transfer experiment. *Bull. Am. Meteorol. Soc.* **88**, 357–374 (2007).
17. D'Asaro, E. A., Sanford, T. B., Niiler, P. P. & Terrill, E. J. Cold wake of hurricane Frances. *Geophys. Res. Lett.* **34**, L15609 (2007).
18. Sanford, T. B., Price, J. F. & Garton, J. B. Upper-ocean response to Hurricane Frances (2004) observed by profiling EM-APEX floats. *J. Phys. Oceanogr.* **41**, 1041–1056 (2011).
19. D'Asaro, E. A. et al. Impact of typhoons on the ocean in the Pacific. *Bull. Am. Meteorol. Soc.* **95**, 1405–1418 (2014).
20. Cione, J. J. The relative roles of the ocean and atmosphere as revealed by buoy air–sea observations in Hurricanes. *Mon. Weather Rev.* **143**, 904–913 (2015).
21. Foltz, G. R., Zhang, C., Meinig, C., Zhang, J. A. & Zhang, D. An unprecedented view inside a hurricane. *Eos* <https://doi.org/10.1029/2022EO220228> (2022).
22. Brizuela, N. G. et al. A vorticity-divergence view of internal wave generation by a fast-moving tropical cyclone: insights from Super Typhoon Mangkhut. *J. Geophys. Res. Oceans* **128**, e2022JC019400 (2023).
23. Wadler, J. B., Cione, J. J., Michlowitz, S., Jaimes de la Cruz, B. & Shay, L. K. Improving the statistical representation of tropical cyclone in-storm sea surface temperature cooling. *Weather Forecast.* **39**, 847–866 (2024).
24. Price, J. F. Upper ocean response to a hurricane. *J. Phys. Oceanogr.* **11**, 153–175 (1981).
25. D'Asaro, E. A. The ocean boundary layer below Hurricane Dennis. *J. Phys. Oceanogr.* **33**, 561–579 (2003).
26. Vincent, E. M. et al. Processes setting the characteristics of sea surface cooling induced by tropical cyclones. *J. Geophys. Res. Oceans* **117**, C02020 (2012).
27. Lin, I. I. et al. New evidence for enhanced ocean primary production triggered by tropical cyclone. *Geophys. Res. Lett.* **30**, 1718 (2003).
28. Huang, P., Lin, I. I., Chou, C. & Huang, R. H. Change in ocean subsurface environment to suppress tropical cyclone intensification under global warming. *Nat. Commun.* **6**, 7188 (2015).
29. Chang, S. W. & Anthes, R. A. The mutual response of the tropical cyclone and the ocean. *J. Phys. Oceanogr.* **9**, 128–135 (1979).
30. Liu, Y. et al. Effect of storm size on sea surface cooling and tropical cyclone intensification in the western north Pacific. *J. Clim.* **36**, 7277–7296 (2023).
31. Wentz, F. J., Gentemann, C., Smith, D. & Chelton, D. Satellite measurements of sea surface temperature through clouds. *Science* **288**, 847–850 (2000).
32. Lumpkin, R., Özgökmen, T. & Centurioni, L. Advances in the application of surface drifters. *Annu. Rev. Mar. Sci.* **9**, 59–81 (2017).
33. Da, N. D., Foltz, G. R. & Balaguru, K. Observed global increases in tropical cyclone-induced ocean cooling and primary production. *Geophys. Res. Lett.* **48**, e2021GL092574 (2021).
34. Sobel, A. H., Held, I. M. & Bretherton, C. S. The ENSO signal in tropical tropospheric temperature. *J. Clim.* **15**, 2702–2706 (2002).
35. Johnson, N. C. & Xie, S. P. Changes in the sea surface temperature threshold for tropical convection. *Nat. Geosci.* **3**, 842–845 (2010).
36. Seager, R. et al. Strengthening tropical Pacific zonal sea surface temperature gradient consistent with rising greenhouse gases. *Nat. Clim. Change* **9**, 517–522 (2019).
37. Bister, M. & Emanuel, K. Dissipative heating and hurricane intensity. *Meteorol. Atmos. Phys.* **65**, 233–240 (1998).
38. Lin, I. I. et al. An ocean coupling potential intensity index for tropical cyclones. *Geophys. Res. Lett.* **40**, 1878–1882 (2013).
39. Vecchi, G. A. & Soden, B. J. Effect of remote sea surface temperature change on tropical cyclone potential intensity. *Nature* **450**, 1066–1070 (2007).
40. Emanuel, K. 100 years of progress in tropical cyclone research. *Meteorol. Mon.* **59**, 15.1–15.68 (2018).
41. Gentemann, C. L., Donlon, C. J., Stuart-Menteth, A. & Wentz, F. J. Diurnal signals in satellite sea surface temperature measurements. *Geophys. Res. Lett.* **30**, 1140 (2003).
42. Sriver, R. L. & Huber, M. Observational evidence for an ocean heat pump induced by tropical cyclones. *Nature* **447**, 577–580 (2007).
43. Brizuela, N. G. et al. Prolonged thermocline warming by near-inertial internal waves in the wakes of tropical cyclones. *Proc. Natl Acad. Sci. USA* **120**, e2301664120 (2023).
44. Camargo, S. J. Global and regional aspects of tropical cyclone activity in the CMIP5 models. *J. Clim.* **26**, 9880–9902 (2013).
45. Chang, P. et al. An unprecedented set of high-resolution earth system simulations for understanding multiscale interactions in climate variability and change. *J. Adv. Model. Earth Syst.* **12**, e2020MS002298 (2020).
46. Trabling, B. C. & Bell, M. M. Understanding error distributions of hurricane intensity forecasts during rapid intensity changes. *Weather Forecast.* **35**, 2219–2234 (2020).
47. Emanuel, K. Tropical cyclones. *Annu. Rev. Earth Planet. Sci.* **31**, 75–104 (2003).
48. Knaff, J. A., Sampson, C. R. & DeMaria, M. An operational statistical typhoon intensity prediction scheme for the western North Pacific. *Weather Forecast.* **20**, 688–699 (2005).
49. Eyring, V. et al. Overview of the Coupled Model Intercomparison Project Phase 6 (CMIP6) experimental design and organization. *Geosci. Model Dev.* **9**, 1937–1958 (2016).
50. Warner, J. C., Armstrong, B., He, R. & Zambon, J. B. Development of a Coupled Ocean–Atmosphere–Wave–Sediment Transport (COAWST) modeling system. *Ocean Modell.* **35**, 230–244 (2010).

Publisher's note Springer Nature remains neutral with regard to jurisdictional claims in published maps and institutional affiliations.

Open Access This article is licensed under a Creative Commons Attribution-NonCommercial-NoDerivatives 4.0 International License, which permits any non-commercial use, sharing, distribution and reproduction in any medium or format, as long as you give appropriate credit to the original author(s) and the source, provide a link to the Creative Commons licence, and indicate if you modified the licensed material. You do not have permission under this licence to share adapted material derived from this article or parts of it. The images or other third party material in this article are included in the article's Creative Commons licence, unless indicated otherwise in a credit line to the material. If material is not included in the article's Creative Commons licence and your intended use is not permitted by statutory regulation or exceeds the permitted use, you will need to obtain permission directly from the copyright holder. To view a copy of this licence, visit <http://creativecommons.org/licenses/by-nc-nd/4.0/>.

© The Author(s) 2026

Methods

TC datasets

Global TC best-track data from 1992 to 2021, distributed by the US National Hurricane Center and Joint Typhoon Warning Center, are obtained from the International Best Track Archive for Climate Stewardship (IBTrACS) database⁵¹. The TC data, including location and intensity (represented by 1-minute maximum wind speeds) information, are provided every 6 hours at the primary synoptic hours (00, 06, 12 and 18 UTC) throughout the lifetime of each TC. The Advanced Dvorak Technique Hurricane Satellite (ADT-HURSAT) dataset generated by ref. 3, which is spatially and temporally homogeneous, is also used to calculate the TC intensity trend and yield a similar result. Intense TCs are principally responsible for damage and mortality⁵², so our study is restricted to TCs with intensity reaching Category 1 or above on the Saffir–Simpson Hurricane Scale. Additionally, TC track points located poleward of 40° N/S and in coastal ocean areas (with water depth shallower than 1,000 m) are pre-excluded^{53,54}. A total of 1,324 Category 1–5 TC cases (17,234 TC track points) are extracted.

Storm-local SST and cooling

Drifters measure SST approximately 10–20 cm beneath the sea surface^{32,55}. Under high insolation and weak winds, the SSTs probably include a diurnal warming signal. However, under TC high winds, the diurnal warming disappears⁴¹. Thus, the drifter-observed SSTs influenced by TCs are foundation SSTs without diurnal warming.

The Drifter Data Assembly Center at the Atlantic Oceanographic and Meteorological Laboratory applies quality control procedures to edit the position and SST observed by drifters and then interpolates them to 6-hour intervals. To determine TC-induced storm-local SST cooling, we search for paired pre-TC SST observations and then subtract them from storm-local SST observations. Detailed criteria are listed: (1) the storm-local SST should be observed at the exact time of TC passage within 500 km of the TC centre; (2) to calculate the storm-local SST cooling (that is, storm-local SST minus the reference pre-TC SST), the pre-TC SST observed 4 to 10 days before TC passage is identified to pair with the storm-local SST; (3) the distance between the paired storm-local SST and pre-TC SST observations should be less than 100 km to minimize the effect of background spatial ocean variability⁵⁶. On the basis of the criteria, 32,801 storm-local SST and cooling observations are identified. Distribution of these storm-local drifter observations captures distribution of global TCs.

Following similar criteria to identify storm-local cooling, TC-induced SST cooling from 5 days before TC passage to 5 days after is further estimated based on drifter observations. We characterize the TC-induced SST cooling through composite analyses. SST cooling data, located within 100 km of TC centres, are averaged to obtain the temporal evolution.

We use different upper-bound distances of 50 km and 150 km to determine the TC-induced SST cooling for composite analyses. The results are consistent with that obtained using the upper-bound distance of 100 km (Extended Data Fig. 2a). Although we impose a limit on the pairing distance between storm-local SST and pre-TC SST, if the instrument crosses a mesoscale ocean feature, such as an eddy, with differing thermal features, the SST cooling could be affected. To examine the potential impact, we add a Lagrangian approach and a current velocity criterion to test the sensitivity of the cooling estimate. In the Lagrangian approach, we limit the TC-perturbed SST and the paired pre-TC SST observations to those measured by the same drifter. The composite result agrees with that obtained without this limitation (Extended Data Fig. 2b). Considering pre-existing mesoscale eddies potentially induce geostrophic current anomaly, we divide the SST cooling into two groups: with fast ($> 0.3 \text{ m s}^{-1}$) or slow ($< 0.3 \text{ m s}^{-1}$) currents accompanying the pre-TC SSTs. The 0.3 m s^{-1} is a mean pre-TC current velocity. Average SST cooling with fast or slow currents is consistent and agrees well with the cooling without a current limit criterion

(Extended Data Fig. 2c). These results suggest that the impacts of mesoscale processes in the composite analysis are negligible.

Daily-averaged cooling by averaging 6-hourly drifter observations to comply with the daily microwave satellite and model output is $-0.67 \pm 0.02 \text{ }^\circ\text{C}$, consistent with that based on 6-hourly observations ($-0.68 \pm 0.04 \text{ }^\circ\text{C}$). This is probably because TC passage times are uniformly distributed (before or after) relative to satellite observations on day 0. Thus, when we compose the cooling based on a large number of samples, the impact of temporal inconsistency is filtered out.

SST in TC-active regions

TC-active regions refer to the areas where climatological SST exceeds $27 \text{ }^\circ\text{C}$ during TC seasons, excluding the equatorial band ($5^\circ \text{ N} - 5^\circ \text{ S}$), the South Atlantic and the southeastern Pacific due to rare TC activities. The TC season is defined as August–October for the northern hemisphere and February–April for the southern hemisphere. Monthly SST from the Ocean Reanalysis System 5 (ORASS, $0.25^\circ \times 0.25^\circ$), European Centre for Medium-range Weather Forecasts (ECMWF) Reanalysis v5 (ERA5, $0.25^\circ \times 0.25^\circ$), Extended Reconstructed Sea Surface Temperature (ERSST, $2^\circ \times 2^\circ$) and Hadley Centre Sea Ice and Sea Surface Temperature (HadISST, $1^\circ \times 1^\circ$) datasets, are employed to calculate the warming trend in TC-active regions. Reasonably changing the TC-active regions and TC seasons does not affect the SST trend or our major conclusions. For instance, the TC-active regions and TC seasons selected in the literature² are tested and yield similar results.

Linear trend detection

The trend analyses are based on normalized values, calculated by subtracting an average value within each basin, following a method described in the literature^{9,10}. By doing so, the influence of intra-basin changes on the global trend is isolated. Linear trend analyses are conducted using ordinary least-squares regression based on the 3-year running average data.

Sensitivity tests are conducted to assess the trend analysis. We reduce drifter samples, keeping the number of samples the same each year and repeat this process 10,000 times. No notable difference is identified. Moreover, we randomly resample the gridded Ocean Reanalysis System 5 (ORASS) SST data according to drifter observations, repeating this process 10,000 times; and then compare the linear trend of the TC-active regional mean SST from these resamples with that from gridded ORASS SST data. A consistent linear trend of the tropical mean SST is identified.

Although a radius of 500 km is a larger area than TCs' inner-core area and there is substantial spatial variability in the storm-local SSTs, it has little influence on the conclusion about the fast-warming storm-local SST trend. We calculate the storm-local SST warming trends using SSTs within 500 km, 300 km and 100 km from TC centres. In these cases, we observed a consistently fast-warming trend. We choose a radius of 500 km to include SST observations beneath TCs as much as possible.

Potential intensity

Potential intensity (PI) is the maximum intensity that a TC can achieve under given SST and atmospheric conditions^{37,38,57}. In this study, PI is calculated based on the storm-local SST,

$$V_{\text{PI}}^2 = \frac{\text{SST} - T_0}{T_0} \frac{C_\kappa}{C_D} (\kappa^* - \kappa) \quad (1)$$

where SST is the storm-local SST, T_0 is the outflow temperature, C_κ is the dimensionless enthalpy transfer coefficient, C_D is the drag coefficient, κ^* is the enthalpy of the ocean surface and κ is the enthalpy of the atmosphere near the surface. The outflow temperature and C_D are determined using the published code calculating the potential intensity (<ftp://texmex.mit.edu/pub/emanuel/TCMAX/>). Specifically, by using sounding data (temperature, humidity and pressure as

functions of altitude), the equilibrium level where the parcel becomes cooler and denser than the surrounding environment and stops rising can be calculated; then the outflow temperature can be determined by averaging the temperatures at and above the equilibrium level. The ratio of C_k to C_D of 0.9 is used.

To calculate TC potential intensity, 6-hourly mean sea-level pressure, air temperature and specific humidity, at 19 isobaric levels (that is, 1,000; 950; 900; 850; 800; 750; 700; 650; 600; 550; 500; 450; 400; 350; 300; 250; 200; 150 and 100 hPa) are used. To ensure consistency with the drifter SST observations, they are interpolated to match the location of drifter SST observations.

PI-derived intensity trend

Following the method proposed in ref. 6, the theoretically expected mean intensity trend of Category 1–5 TCs based on PI trend, is explored. Assuming that PI can be described by an autoregressive process with autocorrelation coefficient r , annual mean μ , standard deviation σ and an increasing trend δ , PI can be formed as

$$PI(t) = \mu + \sigma x(t) + \delta(t) \quad (2)$$

$$x(t) = rx(t - \Delta t) + \sqrt{1 - r^2} \varepsilon(t) \quad (3)$$

where x is a standardized variable with zero mean and standard deviation of unity, r is the lag-1 (Δt) autocorrelation, and ε is the white noise. For Category 1–5 TCs, assuming that TCs have a uniform probability of achieving any mean TC intensity between the minimum Category 1 intensity (that is, 33 m s^{-1}) and the upper-bound intensity that TCs can achieve (that is, PI), synthetic time series of mean TC intensity can be formed as

$$\text{Intensity}(t, \gamma(t)) = \text{Intensity}_{\min} + (PI(t) - \text{Intensity}_{\min})\gamma(t) \quad (4)$$

where $\text{Intensity}_{\min} = 33 \text{ m s}^{-1}$ and $\gamma(t)$ is the random number drawn from a uniform distribution on the interval (0, 1). For each year, the number of $\gamma(t)$ is a random number drawn from a Poisson distribution with the specified rate (global annual number of Category 1–5 TCs, approximately 49). To calculate the trend of mean TC intensity, we use the trend of the mean of the 10,000 subsamples for that expected trend. More details on this idealized experiment can be found in the literature⁶.

Comparing microwave satellite data with drifters

On the basis of drifter observations, we assess the uncertainties of TC-induced storm-local SST cooling observed by microwave satellites. Daily microwave optimally interpolated SST data version 5.0 from Remote Sensing Systems, with roughly 25-kilometre resolution, are used. Because this dataset has been available since 1998, we compare drifter and microwave satellite observations of TC-induced SST cooling from 1998 to 2021.

Although satellite microwave radiometers measure sub-skin SST at several millimetres beneath the surface influenced by diurnal warming, the sub-skin SSTs have been converted to foundation SSTs without diurnal warming by using a diurnal warming model⁴¹. Moreover, the upper ocean from the sea surface to O (100 m) depth is well mixed due to TC-induced strong turbulent vertical mixing^{17,19,24}. Therefore, the difference in measuring depth between microwave satellites and drifters has a negligible influence on SST measurements under TC conditions.

By interpolating the gridded microwave SSTs to the locations of all drifter samples using bilinear interpolation, we obtain the projected microwave satellite observations to calculate the TC-induced SST cooling. Therefore, the comparison of composites between drifter and projected microwave satellite data is based on one-to-one paired data from the same TCs.

TC-induced SST cooling is further calculated based on gridded microwave satellite observations. When comparing the composites

derived from projected and gridded microwave satellite observations, we find no noticeable difference between them (Extended Data Fig. 4). The result suggests that the composite TC-induced SST cooling derived from drifter and projected satellite observations is statistically robust.

We test the overestimation of inner-core SST cooling by microwave satellite data using independent moored buoys (and floats) in global TC-active basins. To identify inner-core SST cooling and maximize sample size, we pair each buoy with tropical depressions and tropical storms within 100 km and Category 1–5 within 500 km from TC centres that passed within the open ocean. In total, 2,078 storm-local observations from 55 buoys that encountered TCs are obtained, sourced from: the global tropical moored buoy array (Tropical Atmosphere Ocean Project, TAO/TRITON; Prediction and Research Moored Array in the Tropical Atlantic, PIRATA; Research Moored Array for African-Asian-Australian Monsoon Analysis and Prediction, RAMA); the National Data Buoy Center buoys; the floats under hurricanes Irma (2017) and Florence (2018); a G2 buoy that deployed in the South China Sea; the Kuroshio Extension Observatory (KEO) buoy; and the Bailong buoy under TC Dahlia (2017).

Enthalpy flux

Total enthalpy flux (Q_t), that is, sensible (Q_s) plus latent (Q_l) heat flux, is estimated using bulk aerodynamic formulas¹⁵,

$$Q_s = \rho_a C_{pa} C_H V (T_s - T_a) \quad (5)$$

$$Q_l = \rho_a L_{va} C_E V (q_s - q_a) \quad (6)$$

$$Q_t = Q_s + Q_l \quad (7)$$

where ρ_a is the air density; C_{pa} is the specific heat of air at constant pressure; L_{va} is the latent heat of vaporization at a given T_a ; C_H and C_E are the dimensionless coefficients of heat and moisture exchange, respectively, which are taken as 1.3×10^{-3} (ref. 58); V is the wind speed of TCs; T_s and T_a are the inner-core SST and near-surface air temperature respectively; q_s and q_a are the saturation mixing ratio at the inner-core SST and the actual mixing ratio of the air, respectively. In this work, the enthalpy flux is estimated using drifter SST observations and projected microwave satellite SST observations, respectively. Then, the enthalpy flux bias based on microwave satellite SST observations is estimated through a comparison with that based on drifter observations. Given that the wind speeds of TCs are generally spatially asymmetrical, the enthalpy flux calculated in this study, based on the maximum wind speed of TCs, may represent the upper bound of the spatial distribution of enthalpy flux.

Model simulations

Average inner-core SST cooling is evaluated in the HighResMIP experiments. The HighResMIP is an integral part of CMIP6, with the primary objective of enhancing the models' capability by improving their horizontal resolutions. For each simulated TC centre, inner-core SST cooling is calculated within 100 km of TC centres on the day of TC passage.

In HighResMIP experiments, storm tracks from five models—Euro-Mediterranean Centre on Climate Change coupled climate model (CMCC-CM2), Centre National de Recherches Météorologiques model version 6 (CNRM-CM6-1), PProcess-based climate sIMulation: AdVances in high-resolution modeling and European climate Risk Assessment (PRIMAVERA) version of European Community Earth System Model (EC-Earth-3P), European Centre for Medium-Range Weather Forecasts-Integrated Forecasting System (ECMWF-IFS) and Hadley Centre Global Environmental Model 3—Global Coupled configuration 3.1 (HadGEM3-GC31)—are provided. These storm tracks are calculated using the 'TRACK' storm tracking algorithm⁵⁹. The corresponding daily SST data are then utilized to calculate simulated inner-core SST cooling. Horizontal resolution of the SST data from HadGEM3-GC31

is 50 km, whereas that of the others is 25 km. We utilize the simulated data derived from historical experiments (hist-1950). Although the simulated data in the hist-1950 span from 1950 to 2014, we focus on the period between 1992 and 2014, covered by drifter observations.

The Coupled Ocean-Atmosphere-Wave-Sediment Transport Model (COAWST) modelling system consists of the Weather Research and Forecasting (WRF) as the atmospheric model, the Regional Ocean Modeling System (ROMS) as the oceanic model and the Simulating Waves Nearshore as the wave model. In this study, the WRF and ROMS coupling model are employed. Resolutions of both the WRF and ROMS models adopt identical grids with a horizontal resolution of 9 km. WRF has 39 vertical levels. Physical parameterization schemes in WRF include the Lin scheme for microphysics⁶⁰, the Modified Tiedtke scheme for Cumulus convection⁶¹, the University of Washington scheme for the planetary boundary layer⁶² and the Monin–Obukhov (Janjic) scheme for the surface layer⁶³. The ROMS model has 40 vertical levels. The Mellor–Yamada vertical mixing scheme is used in the simulation. By using the Model Coupling Toolkit, the exchange of environmental data between WRF and ROMS is achieved. The WRF and ROMS coupling model has been widely used for TC simulations^{12,54}.

We simulate 22 TC cases for control runs, comprising 486 6-hourly recorded track points across Category 1–5 in the WNP. The simulation generates approximately 2,000 hourly model outputs. For experimental runs, we re-forecast these TCs with a reduced inner-core SST cooling for the ocean component of the modelling system. We reduce inner-core SST cooling by reducing vertical mixing, which dominates TC-induced SST cooling²⁴, with all other conditions remaining unchanged. By comparing inner-core SST cooling and TC intensity between the control and experimental runs, we can isolate the effect of overcooling on TC intensity simulations. Uncertainty analysis is carried out using the Monte Carlo method¹².

Overcooling in CMIP6 high-resolution models

Our analysis compares aggregated attributes from all observed TCs against those from thousands of TCs in climate models. In this regard, the impact from inter-event differences in TC attributes can be virtually averaged out, except for that from the underestimated TC intensity in the climate models, because it is a common bias. Despite the underestimation of modelled TC intensity, cooling is overestimated. The overcooling by models would probably be even more pronounced if the models were capable of reproducing higher TC intensities as observed in nature. Limited by this overcooling, and other factors such as low model resolution and uncertainties in model physics and parameterizations^{64,65}, climate models can hardly reproduce intense TCs as observed.

As such, we use Category 1 TCs located in the WNP TC main development region for a comparison. Four of five models (except a few Category 1 TCs in the EC-Earth3P model) reproduce track densities of Category 1 TCs as those in best track records with drifter observations (Extended Data Fig. 8a–f). These climate models also reproduce translation speeds of TCs. In CMCC-CM2, CNRM-CM6-1 and HadGEM3-GC31, the average translation speeds of simulated TCs are consistent with observations in the best-track dataset, with a small bias of no more than 0.08 m s⁻¹. One exception is that the ECMWF-IFS model produces TCs with a faster average translation speed (6.98 m s⁻¹) than that of best-track TCs (5.12 m s⁻¹). However, this faster translation speed in the ECMWF-IFS model should have resulted in less cooling than observations, but the overcooling is still produced. Thus, under the same TC intensity (Category 1), these models produce an overestimate of the TC-induced cooling, statistically significant above the 95% confidence level (Extended Data Fig. 8g). The multi-model ensemble mean for slow TCs shows a more than 80% overestimate, and for fast TCs, there is an overestimate of about 150%. We further analysed the cooling bias under different TC intensities in the WNP main development region using output from the CNRM-CM6-1 model. This model is selected

because it successfully simulates TCs from Tropical Depression to Category 4, while other models fail to simulate Category 3–5 TCs. We find that overcooling consistently occurs for individual TC intensities (Extended Data Fig. 8h).

Data availability

Global tropical cyclone best-track data are available at <https://climatedataguide.ucar.edu/climate-data/ibtracs-tropical-cyclone-best-track-data>. Advanced Dvorak Technique–Hurricane Satellite data are available at <https://www.pnas.org/doi/suppl/10.1073/pnas.1920849117>. Six-hourly drifter sea surface temperature data are available from the Global Drifter Program at <https://www.aoml.noaa.gov/phod/gdp/data.php>. Daily microwave satellite sea surface temperature data are available from the Remote Sensing Systems at <https://www.remss.com>. Global tropical moored buoys are available at <https://www.pmel.noaa.gov/tao/drupal/disdel/>. National Data Buoy Center buoys are available at <https://www.ndbc.noaa.gov/>. Floats are downloaded from <https://agupubs.onlinelibrary.wiley.com/doi/full/10.1029/2019AV000161>. KEO buoy are available at <https://www.pmel.noaa.gov/ocs/data/disdel/>. Bailing buoy data are downloaded from <https://www.sciencedirect.com/science/article/pii/S037702652030124X>. Ocean Reanalysis System 5 monthly sea surface temperature data are available at <https://www.ecmwf.int/en/forecasts/dataset/ocean-reanalysis-system-5>. ECMWF Reanalysis v5 atmospheric variable and SST data are available at <https://www.ecmwf.int/en/forecasts/dataset/ecmwf-reanalysis-v5>. Extended Reconstructed Sea Surface Temperature data are available at <https://www.ncei.noaa.gov/pub/data/cmb/ersst/v5/netcdf/>. Hadley Centre Sea Ice and Sea Surface Temperature data are available <https://www.metoffice.gov.uk/hadobs/hadisst/>. Daily sea surface temperature data from CMIP6 models are available at <https://esgf.ceda.ac.uk>, and corresponding tropical cyclone data are available at https://data.ceda.ac.uk/badc/highresmip-derived/data/storm_tracks/TRACK. Data used for plotting the figures in the paper are available via figshare at <https://doi.org/10.6084/m9.figshare.30464234> (ref. 66).

Code availability

Codes used to create the figures are available via figshare at <https://doi.org/10.6084/m9.figshare.30464285> (ref. 67).

References

- Knapp, K. R., Kruk, M. C., Levinson, D. H., Diamond, H. J. & Neumann, C. J. The international best track archive for climate stewardship (IBTrACS) unifying tropical cyclone data. *Bull. Am. Meteor. Soc.* **91**, 363–376 (2010).
- Peduzzi, P. et al. Global trends in tropical cyclone risk. *Nat. Clim. Change* **2**, 289–294 (2012).
- Foltz, G. R., Balaguru, K. & Hagos, S. Interbasin differences in the relationship between SST and tropical cyclone intensification. *Mon. Weather Rev.* **146**, 853–870 (2018).
- Glenn, S. M. et al. Stratified coastal ocean interactions with tropical cyclones. *Nat. Commun.* **7**, 10887 (2016).
- Lumpkin, R. & Centurioni, L. Global Drifter Program quality-controlled 6-hour interpolated data from ocean surface drifting buoys (version buoydata_15001_dec21). NOAA National Centers for Environmental Information <https://doi.org/10.25921/7ntx-z961> (2022).
- Park, J. J., Kwon, Y.-O. & Price, J. F. Argo array observation of ocean heat content changes induced by tropical cyclones in the north Pacific. *J. Geophys. Res.* **116**, C12025 (2011).
- Sobel, A. H. et al. Human influence on tropical cyclone intensity. *Science* **353**, 242–246 (2016).
- Zhang, J. A., Black, P. G., French, J. R. & Drennan, W. M. First direct measurements of enthalpy flux in the hurricane boundary layer: the CBLAST results. *Geophys. Res. Lett.* **35**, L14813 (2008).

59. Roberts, M. CMIP6 HighResMIP: tropical storm tracks. *Centre for Environmental Data Analysis* <http://catalogue.ceda.ac.uk/uuid/e82a62d926d7448696a2b60c1925f811> (2019).
60. He, Y., Kun, Y., Tandong, Y. & Jie, H. Numerical simulation of a heavy precipitation in Qinghai-Xizang Plateau based on WRF model. *Plateau Meteorol.* **31**, 1183–1191 (2012).
61. Zhang, C., Wang, Y. & Hamilton, K. Improved representation of boundary layer clouds over the southeast pacific in ARW–WRF using a modified Tiedtke cumulus parameterization scheme. *Mon. Weather Rev.* **139**, 3489–3513 (2011).
62. Bretherton, C. S. & Park, S. A new moist turbulence parameterization in the community atmosphere model. *J. Clim.* **22**, 3422–3448 (2009).
63. Monin, A. S. & Obukhov, A. M. Basic laws of turbulent mixing in the atmosphere near the ground. *Geofiz. Akad. Nauk SSSR* **24**, 1963–1987 (1954).
64. Rios-Berrios, R. & Torn, R. D. Climatological analysis of tropical cyclone intensity changes under moderate vertical wind shear. *Mon. Weather Rev.* **145**, 1717–1738 (2017).
65. Wang, W. et al. Improving the intensity forecast of tropical cyclones in the hurricane analysis and forecast system. *Weather Forecast.* **38**, 2057–2075 (2023).
66. Huang, M. & Guan, S. Data for published paper entitled 'weak self-induced cooling of tropical cyclones amid fast sea surface warming'. *figshare* <https://doi.org/10.6084/m9.figshare.30464234> (2025).
67. Huang, M. & Guan, S. Code for published paper entitled 'Weak self-induced cooling of tropical cyclones amid fast sea surface warming'. *figshare* <https://doi.org/10.6084/m9.figshare.30464285> (2025).

Acknowledgements

This work is supported by the National Natural Science Foundation of China (grant number 92258301 to J.T.), the National Key Research and

Development Program of China (grants numbers 2023YFF0805200 and 2022YFC3104304 to X.L. and S.G.). S.G. is further supported by the National Natural Science Foundation of China (grant number 42476029).

Author contributions

S.G., I.-I.L., Z.Z. and W.Z. conceived the central idea, and W.C. modified the idea. S.G., I.-I.L. and L.Z. designed the analysis. M.H. performed the analysis and generated the figures. S.G., M.H., I.-I.L. and L.Z. drafted the manuscript. W.C. substantially revised the manuscript. Z.X. and X.L. performed the COAWST model experiments, and M.H. analysed the model outputs. W.Z. and J.T. led the research and improved the manuscript. J.T., F.-F.J., W.M., H.-S.K., Q.W., C.Z. and Z.M. discussed the results and commented on the manuscript. All authors discussed the results and approved the submitted version.

Competing interests

The authors declare no competing interests.

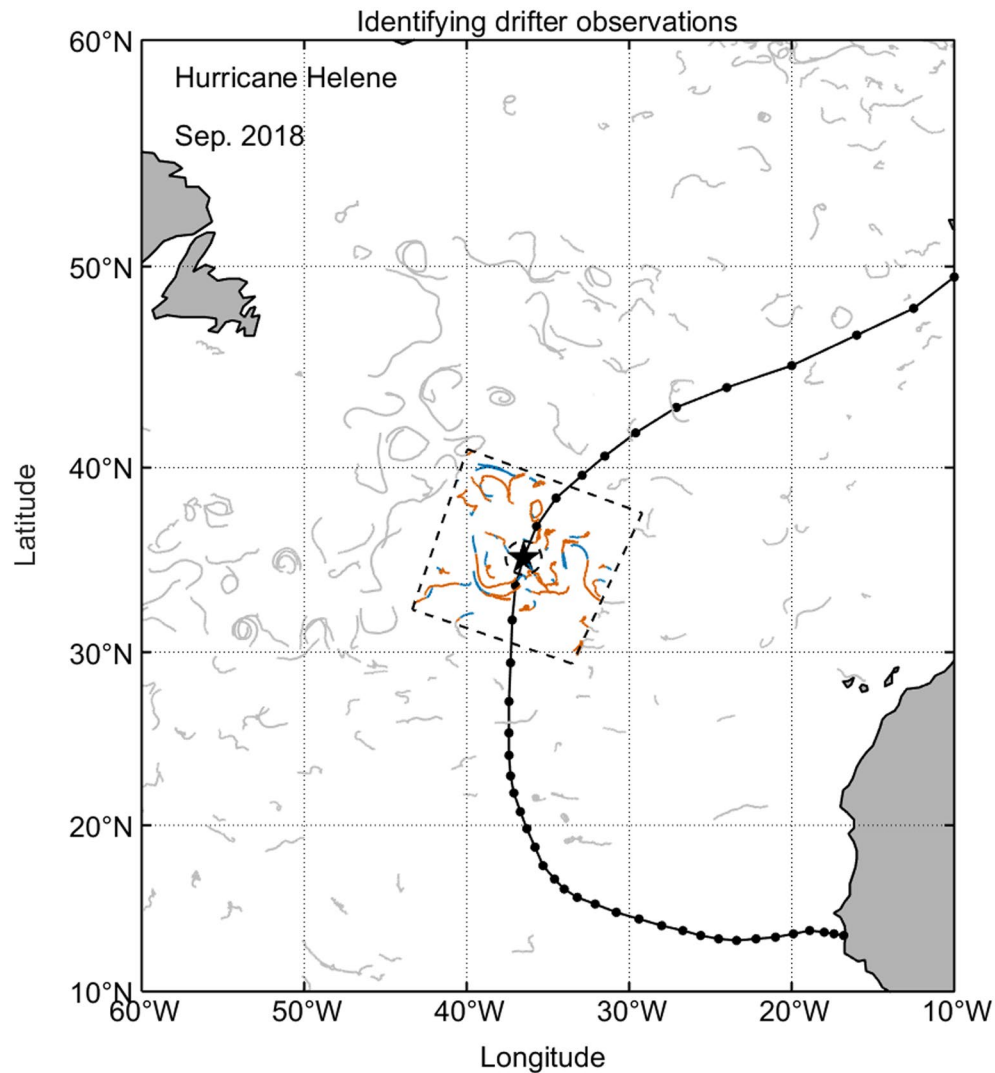
Additional information

Extended data is available for this paper at <https://doi.org/10.1038/s41561-025-01879-x>.

Correspondence and requests for materials should be addressed to Wenju Cai, I-I Lin or Wei Zhao.

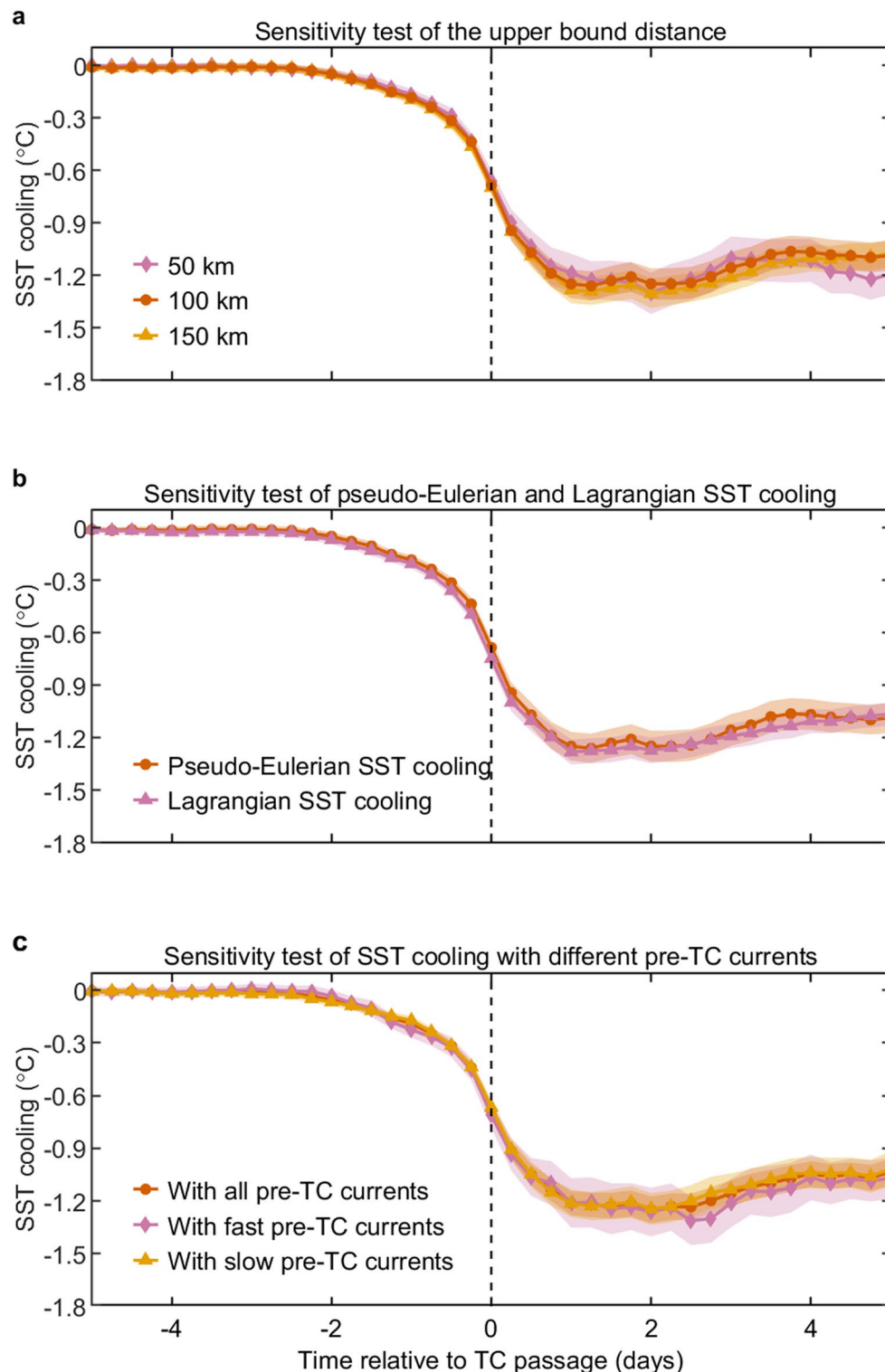
Peer review information *Nature Geoscience* thanks Noel Gutierrez-Brizuela and the other, anonymous, reviewer(s) for their contribution to the peer review of this work. Aliénor Lavergne, Tom Richardson, James Super, in collaboration with the *Nature Geoscience* team.

Reprints and permissions information is available at www.nature.com/reprints.



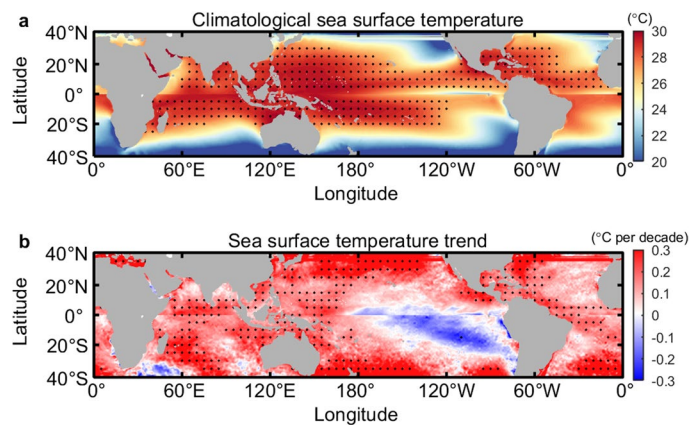
Extended Data Fig. 1 | Method for identifying drifter observations under tropical cyclones, using Hurricane Helene (2018) as an example. Black solid line with dots represents 6-hourly best-track data of Hurricane Helene. Black star highlights a specific track point. Dashed box outlines a domain selected for spatial composite analyses. Dashed circle represents the inner-core area. Blue lines show drifter trajectories with sea surface temperature observations from 4 days to 10 days before the Hurricane's passage, serving as reference

pre-hurricane SST. Red lines indicate drifter SST observations collected from 5 days before to 5 days after the Hurricane's passage, used to determine sea surface temperature cooling. Grey lines trace other drifters' paths during the same period that are not within the specified domain. We illustrate the method for identifying drifter observations corresponding to a 6-hourly tropical cyclone track point. Basemap generated using M_Map v1.4 (www.eoas.ubc.ca/~rich/map.html).



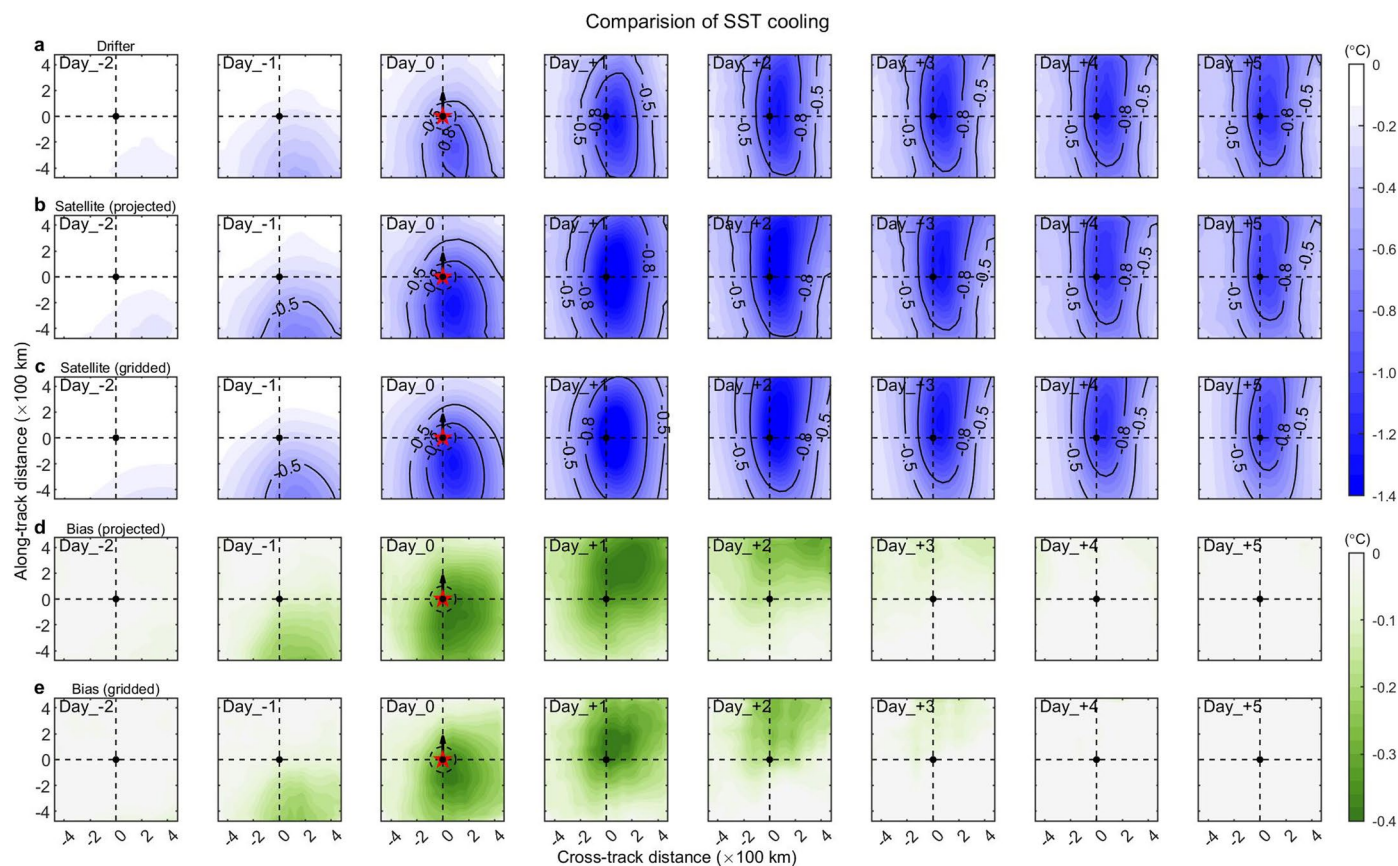
Extended Data Fig. 2 | Sensitivity tests on impacts from an upper bound distance and mesoscale processes. **a**, Temporal evolution of composite sea surface temperature (SST) cooling using different upper bound distances for paired SSTs: 50 km (pink line), 100 km (red line), and 150 km (yellow line). **b**, Red line corresponds to the result based on the pseudo-Eulerian paired SSTs. Pink line represents SST cooling estimated by requiring paired SSTs to come from measurements by the same drifter, thereby strictly adhering to Lagrangian SST

measurements that follow water parcels. **c**, Red, pink, and yellow lines denote SST cooling with all, fast, and slow pre-TC (tropical cyclone) currents, respectively. In all panels, lines and shaded areas denote mean cooling averaged within 100 km from storm centers and corresponding 95% confidence intervals. Vertical dashed lines indicate the time of TC passage. Little differences are found in these sensitivity tests, indicating that the upper bound distance is appropriate and the impact of mesoscale processes is negligible.



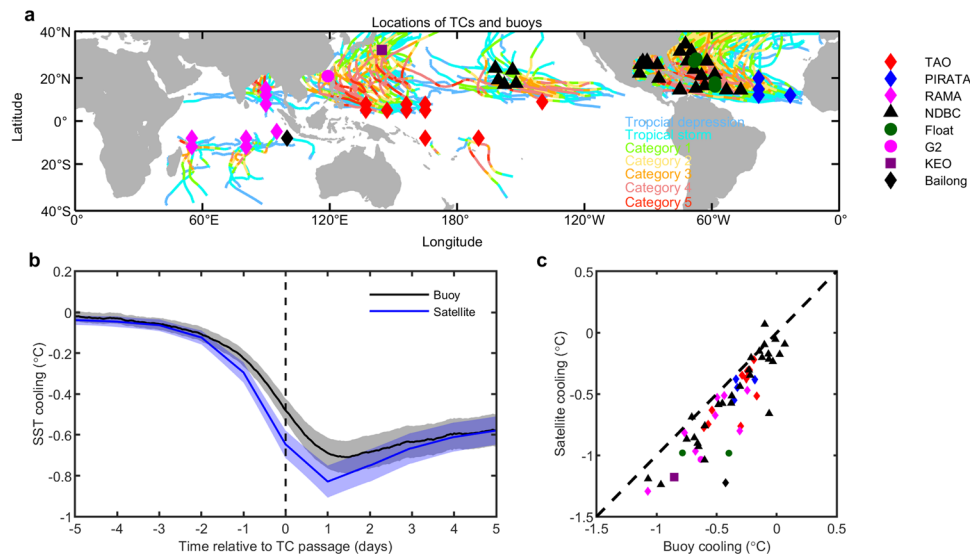
Extended Data Fig. 3 | Spatial pattern of climatological sea surface temperature and its trend over 1992–2021. a, Climatological sea surface temperature during tropical cyclone seasons over 1992–2021 from the ORASS dataset. The tropical cyclone season is defined as August–October for the Northern Hemisphere and February–April for the Southern Hemisphere. Black dots denote tropical cyclone-active regions where climatological sea surface temperature > 27 °C, excluding the equatorial band 5°N–5°S, the South Atlantic,

and the southeastern Pacific with rare tropical cyclones. **b**, The corresponding sea surface temperature trend during tropical cyclone seasons. Black dots denote that the warming trends are statistically significant at the 95% confidence level based on a two-sided Student's *t*-test. The spatial patterns of climatological sea surface temperature and trend are consistent in the ERA5, ERSST, and HadISST datasets. Basemaps generated using M_Map v1.4 (www.eoas.ubc.ca/~rich/map.html).



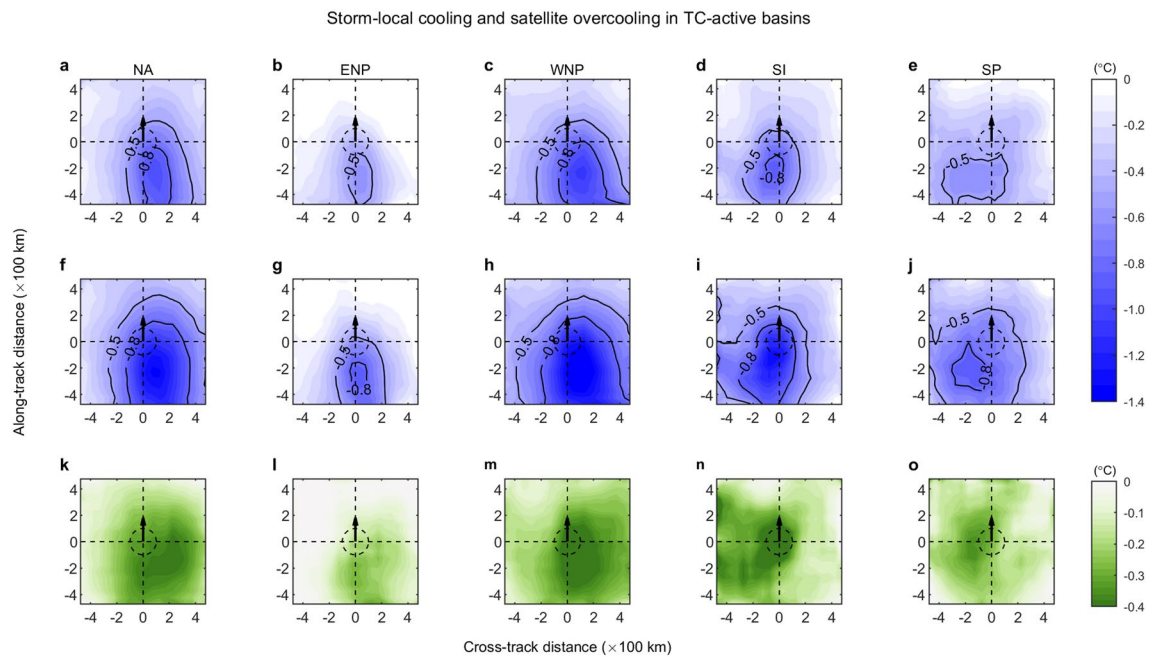
Extended Data Fig. 4 | Comparison of sea surface temperature cooling induced by tropical cyclones between drifter and microwave satellite composites. **a**, Composites of sea surface temperature (SST) cooling based on drifter observations from 2 days before (Day₋₂) to 5 days after (Day₊₅) tropical cyclone passage in the northern hemisphere. Black dots denote recorded tropical cyclone locations. On Day₀, star denotes tropical cyclones reaching the recorded locations, arrow denotes the cyclone's moving direction, and dashed circle denotes the inner-core area. **b,c**, Same as **(a)**, but based on projected and

gridded microwave satellite observations, respectively. **d,e**, Same as **(a)**, but for cooling bias estimated from projected and gridded microwave satellite observations, respectively. Microwave satellites can accurately capture cold wakes 2–3 days after tropical cyclones, but struggle to observe inner-core cooling during tropical cyclones. Consistency between composites based on projected and gridded microwave satellite observations suggests that drifter sampling can be used to statistically characterize the tropical cyclone-induced cooling.



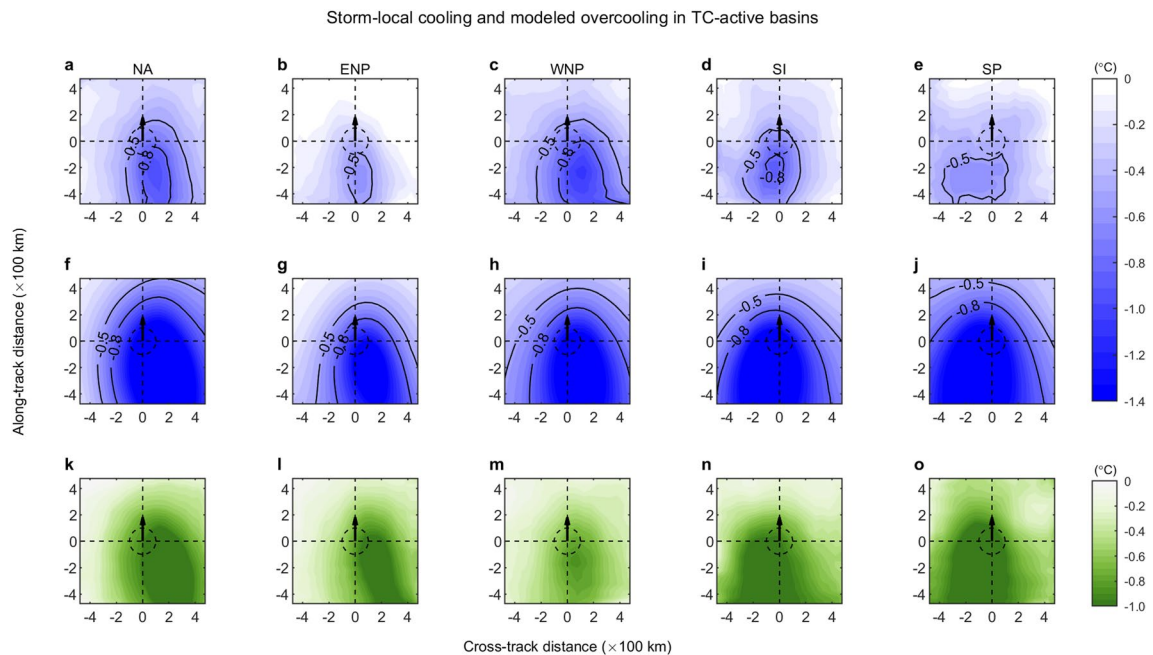
Extended Data Fig. 5 | Comparison of inner-core cooling between moored buoys and microwave satellites. a, Global map of sampling locations, showing tracks of the sampled tropical cyclones and positions of moored buoys and floats. **b**, Time series of mean inner-core sea surface temperature (SST) cooling from moored buoys (black) and corresponding microwave satellites (blue). Lines and shaded areas denote mean cooling and corresponding 95% confidence intervals. Vertical dashed line indicates the time of TC passage; the cooling value at this point defines the inner-core cooling. **c**, Scatterplot of inner-core cooling

observed by each buoy against the cooling from the corresponding microwave satellite data. 1:1 line (black dashed) is shown for reference. The dataset comprises 2,078 storm-local observations from 55 buoys that encountered tropical cyclones, sourced from: the TAO, PIRATA, and RAMA buoys; the NDBC buoys; the floats under Hurricanes Irma (2017) and Florence (2018); a G2 buoy in the South China Sea; the KEO buoy; and the Bailong buoy under TC Dahlia (2017). Basemaps in **a** generated using M_Map v1.4 (www.eoas.ubc.ca/~rich/map.html).



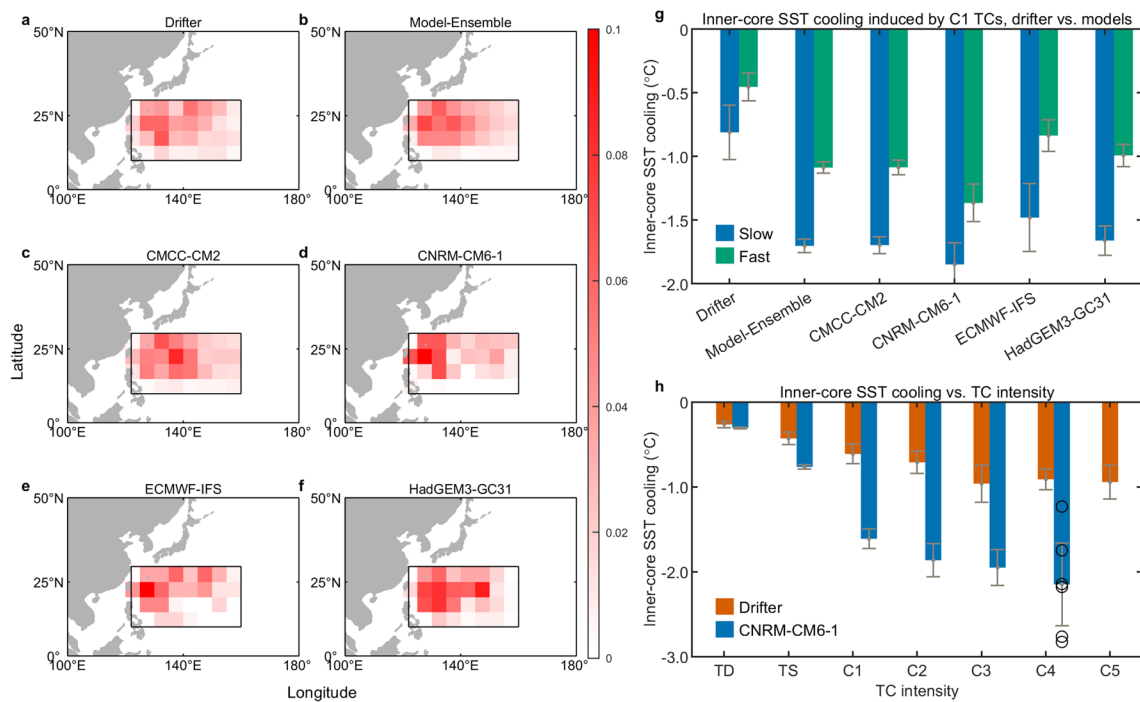
Extended Data Fig. 6 | Overcooling in microwave satellite observations in individual tropical cyclone basins. **a–e**, Composites of storm-local sea surface temperature cooling derived from drifter observations in the North Atlantic (NA), Eastern North Pacific (ENP), Western North Pacific (WNP), South Indian (SI), and South Pacific (SP). The North Indian is not considered as it has a small number of Category 1–5 tropical cyclones recorded. Contours of -0.5°C and

-0.8°C are shown, with arrows denoting cyclones' moving direction and dashed circles denoting the inner-core area. **f–j**, Same as (**a–e**), but derived from projected microwave satellite observations. **k–o**, Same as (**a–e**), but for cooling bias estimated from projected microwave satellite observations. Inner-core overcooling in microwave satellite observations exists in individual tropical cyclone-active basins.



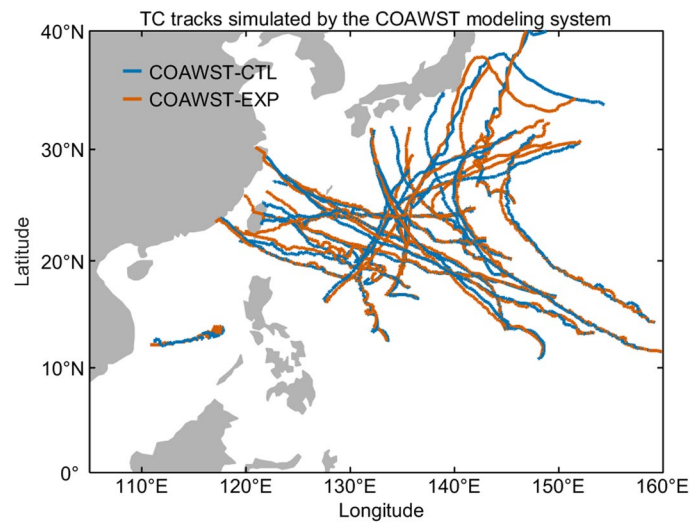
Extended Data Fig. 7 | Overcooling in CMIP6 models in individual tropical cyclone basins. **a–e**, Composites of storm-local sea surface temperature cooling derived from drifter observations in the North Atlantic (NA), Eastern North Pacific (ENP), Western North Pacific (WNP), South Indian (SI), and South Pacific (SP). The North Indian is not considered as it has a small number of Category 1–5 tropical cyclones recorded. Contours of -0.5°C and -0.8°C are shown,

with arrows denoting cyclones' moving direction and dashed circles denoting the inner-core area. **f–j**, Same as **(a–e)**, but derived from the climate models. **k–o**, Same as **(a–e)**, but for the modeled cooling bias. Modeled overcooling in individual tropical cyclone-active basins is simulated by CMIP6 high-resolution climate models.



Extended Data Fig. 8 | Sensitivity tests examining dependences of modeled overcooling on tropical cyclone track density, translation speed, and intensity. **a**, Category 1 tropical cyclones (TCs) track density captured by drifter observations in the Western North Pacific TC main development region (black box), denoted by dividing number of TCs in each $5^{\circ} \times 5^{\circ}$ by total number of TCs. **b-f**, Same as (a), but simulated by the models. **g**, Inner-core sea surface temperature (SST) cooling induced by slow (blue, $< 5 \text{ m s}^{-1}$) and fast (green, $> 5 \text{ m s}^{-1}$) Category 1 TCs observed by drifters and simulated by models. The inner-core cooling by Drifter, Model-Ensemble, CMCC-CM2, CNRM-CM6-1, ECMWF-IFS, and HadGEM3-GC31 is calculated from 53, 1245, 834, 171, 53, and 187 samples for slow-moving TCs and 67, 1156, 692, 166, 96, and 202 samples for fast-moving TCs. **h**, Inner-core cooling induced by tropical depression (TD), tropical storm (TS),

Category 1–4 (C1–C4) from drifters (red) and the CNRM-CM6-1 high-resolution model (blue). The maximum TC intensity simulated by the model is C4. The inner-core cooling induced by TD, TS, C1, C2, C3, C4, and C5 TCs is calculated from 402, 265, 120, 91, 59, 121, and 45 drifter samples and 7154, 2616, 337, 92, 58, 6, and 0 model samples. 6 samples under C4 TCs for the model are plotted using black circles. In (g, h), bars and error bars indicate mean inner-core cooling and corresponding 95% confidence intervals. Models simulate reasonably well the track density of Category 1 TC observed. Under the same TC attributes, modeled overcooling is produced. The overcooling consistently occurs across TCs from tropical depression to Category 4. Basemaps in a–f generated using M_Map v1.4 (www.eoas.ubc.ca/~rich/map.html).



Extended Data Fig. 9 | Tropical cyclone tracks simulated by the COAWST modeling system. Blue lines represent TC tracks in control (COAWST-CTL) runs without a reduced inner-core sea surface temperature cooling, whereas red lines represent tracks in experimental (COAWST-EXP) runs with a reduced

inner-core sea surface temperature cooling. TC tracks in the COAWST-EXP runs align closely with those in the COAWST-CTL runs. Basemap generated using M_Map v1.4 (www.eoas.ubc.ca/~rich/map.html).

Extended Data Table 1 | Dependence of globally averaged inner-core cooling and cold bias in microwave satellites on tropical cyclone intensity

Intensity	Drifter-observed cooling	Satellite- observed cooling	Cold bias	Overestimation
Category 3–5	-0.83 ± 0.04 °C	-1.20 ± 0.05 °C	-0.37 ± 0.04 °C	45%
Category 1–2	-0.60 ± 0.02 °C	-0.97 ± 0.04 °C	-0.36 ± 0.03 °C	60%
Tropical storm	-0.40 ± 0.03 °C	-0.61 ± 0.03 °C	-0.21 ± 0.03 °C	53%
Tropical depression	-0.21 ± 0.03 °C	-0.27 ± 0.03 °C	-0.06 ± 0.03 °C	29%

Inner-core sea surface temperature cooling is obtained using both drifter and projected microwave satellite observations. Cold bias of microwave satellite observations is represented by mean \pm the 95% confidence intervals. Percentage of overestimation by microwave satellite observations is also listed.